GDCh Research Article Angewandte International Edition Chemie www.angewandte.org

How to cite: Angew. Chem. Int. Ed. 2024, e202422047
doi.org/10.1002/anie.202422047

Zinc-Sulfur Batteries

Engineering Electrolyte Network Structure for Improved Kinetics and Dendrite Suppression in Zn-S Batteries

Yinfeng Guo, Xiaoqing Zhu, Jia Zhang, Tao Zhang, Zilong Wang, Minghui Shan, Fei Wang, Changyong Chase Cao, Guiyin Xu,* and Meifang Zhu*

Abstract: Aqueous zinc-sulfur batteries (Zn–S) are promising alternatives to conventional lithium-ion technology due to their high energy density, low cost, and enhanced safety. However, challenges such as slow redox kinetics of sulfur cathode conversion and inadequate anode stability persist. This study demonstrates that by tuning the electrolyte structure with the introduction of propylene glycol methyl ether (PM) as a co-solvent and ZnI_2 as an electrolyte additive, and significant improvements at both electrodes could be achieved. Experimental and theoretical calculations reveal that the larger polar –OH and C–O–C electron-donating groups in the PM molecule can donate electrons for the redox reaction of I^-/I_3^-. Its role as a redox mediator improves the reversibility of the sulfur cathodic transformation. Additionally, the dipole moment induced by the hydroxyl groups in PM enhances electron transfer from the zinc anode to the electrolyte and promote the decomposition of anions (OTF^-), improving the interfacial stability of the zinc anode. The synergistic effect of PM and the I^-/I_3^- redox mediator pair enables the zinc-sulfur battery to deliver an impressive capacity of 1456 mAh g^{-1} and a high energy density of 471.8 Wh kg^{-1} at a current density of 0.2 A g^{-1}.

[*] Y. Guo, X. Zhu, J. Zhang, T. Zhang, M. Shan, G. Xu, M. Zhu
State Key Laboratory for Modification of Chemical Fibers and Polymer Materials, and College of Materials Science and Engineering, Donghua University, Shanghai, 201620 China
E-mail: xuguiyin@dhu.edu.cn

Z. Wang
Department of Mechanical and Aerospace Engineering, The Hong Kong University of Science and Technology, Clear Water Bay, Kowloon, Hong Kong S.A.R., China

F. Wang
Department of Materials Science, Fudan University, Shanghai 200433, China

C. C. Cao
Laboratory for Soft Machines & Electronics, Department of Mechanical and Aerospace Engineering, Case Western Reserve University, Cleveland, OH 44106, USA
E-mail: ccao@case.edu

Introduction

Rechargeable aqueous zinc batteries (AZIBs) have emerged as a promising candidate for stationary energy storage systems due to their reliable safety, environmental friendliness, abundant resource availability. Furthermore, the zinc metal anode possesses a high theoretical capacity (820 mAh g^{-1}, 5845 mAh cm^{-3}) and a suitable electrochemical potential (−0.76 V vs. standard hydrogen electrode).[1] The high cost and complex fabrication processes of transition metal oxide cathode materials and organic cathode materials have spurred the exploration of other sustainable and alternative cathode materials to meet the demands of AZIBs technology.[2] Moreover, these materials face challenges such as underwhelming structural instability due to their complex valent and phase transitions during reactions. With the considerable theoretical capacity (1672 mAh g^{-1}) and ample sulfur resources available on Earth, elemental sulfur has emerged as a promising option for innovative cathode materials in sulfur-based electrochemical applications, including aqueous zinc-sulfur batteries.[3] The development of aqueous zinc-sulfur batteries offers a balanced solution for modern energy storage systems in terms of safety, high energy density, and environmental friendliness.

The widespread application of organic solvents in sulfur-based batteries leads to drawbacks such as low ionic conductivity and high cost. Moreover, the persistent polysulfide shuttling issue severely compromises the performance of these batteries.[4] For aqueous zinc-sulfur batteries, a theoretical potential of 1.01 V (vs. SHE) based on the conversion reaction between S and ZnS ensures proper operation within the electrochemical window of the aqueous phase system.[5] Unlike other sulfur-based batteries, the special solid-solid reaction conversion mechanism provides a polysulfide-free system that avoids irreversible loss of active material in the cell due to the shuttle effects, degradation of cell life, and low Coulombic efficiency.[6] However, the study of sulfur cathodes in aqueous zinc-sulfur battery system is still at a nascent stage, and many problems remain to be solved: (1) Both sulfur (S) and its discharge product, zinc sulfide (ZnS), exhibit extremely low conductivity (5×10^{-28} S m^{-1} for S and 10^{-9} S m^{-1} for ZnS), effectively acting as insulators for both electrons and ions.[7] (2) The direct solid-solid transition of the S cathode in an aqueous electrolyte leads to slow kinetics.[8] (3) The poor wettability of the aqueous medium to the sulfur electrode can hinder the migration of zinc ions in the cathode, leading to a huge

polarization.[9] (4) The disproportionation of ZnS during the charging process leads to the formation of irreversible sulfates in the aqueous electrolyte, resulting in the loss of sulfur-active materials.[10] In addition, the lifetime of zinc-sulfur aqueous batteries is closely related to the state of the zinc anode. Problems such as the dendrite growth induced by the uneven deposition of Zn^{2+}, corrosion of zinc metal, and hydrogen precipitation caused by H_2O can seriously reduce the stability of the zinc-metal anode, ultimately leading to the equipment failure (Scheme 1). Therefore, designing effective methods to stabilize both the cathode and anode is critical for the development of aqueous zinc-sulfur batteries.

Currently, electrolyte engineering for zinc-sulfur batteries focuses on two key areas: (1) introducing additives to inhibit the zinc anode corrosion, thereby improving the interfacial stability, and (2) incorporating redox mediators to optimize the electrolyte, enhancing the reversibility of the sulfur cathode. For example, Chang *et al.* weakened the bond energy of the Zn–S bond by adding thiourea to increase the diffusion coefficient of zinc ions and decrease the polarization, leading to enhanced charge transfer kinetics in the electrolyte, thus improving the reaction kinetics of ZnS to S.[11] In early studies, the stability of zinc anodes in zinc-sulfur batteries was improved by designing electrolytes. Cui *et al.* designed a low-cost deep eutectic electrolyte composed of urea and choline chloride, featuring high ionic conductivity and a wide electrochemical window. This electrolyte effectively mitigated side reactions and zinc dendrite formation.[3d] Zhu et al. developed a 'cocktail-optimized' electrolyte comprising tetraglyme and water as a cosolvent with iodine (I_2) as a redox mediator. This formulation synergistically enhanced sulfur conversion and suppressed undesirable by-products. However, the capacity of the sulfur cathode is still capped at 1200 mAh g^{-1}, representing less than 75 % of its theoretical capacity.[12] Sun et al. introduced a dual-medium electrolyte based on trimethylammonium benzene iodide ($Me_3PhN^+I^-$), where the R_4N^+ cation acts as a solvation medium. This system alters the sulfur cathodic transition pathway from solid-solid to solid-liquid-solid, improving reaction kinetics and reversibility. However, the effect of electrolyte design on the stability of zinc anodes has not yet been systematically explored.[13] Therefore, introducing a small amount of co-solvent and redox mediators into aqueous zinc-sulfur batteries is an effective way to further enhance the electrochemical performance while ensuring the safety.

In this work, we study the challenges at both electrodes by tuning the electrolyte structure. Through the experiment and computation discussion, we demonstrate that by introducing low-cost and high reduction stability propylene glycol methyl ether (PM) as a co-solvent and zinc iodide (ZnI_2) as an electrolyte additive for zinc-sulfur batteries provides a good catalytic effect on the solid-solid conversion at the sulfur cathode. The terminal –OH and C–O–C of PM are electron-donating groups, which can provide electrons

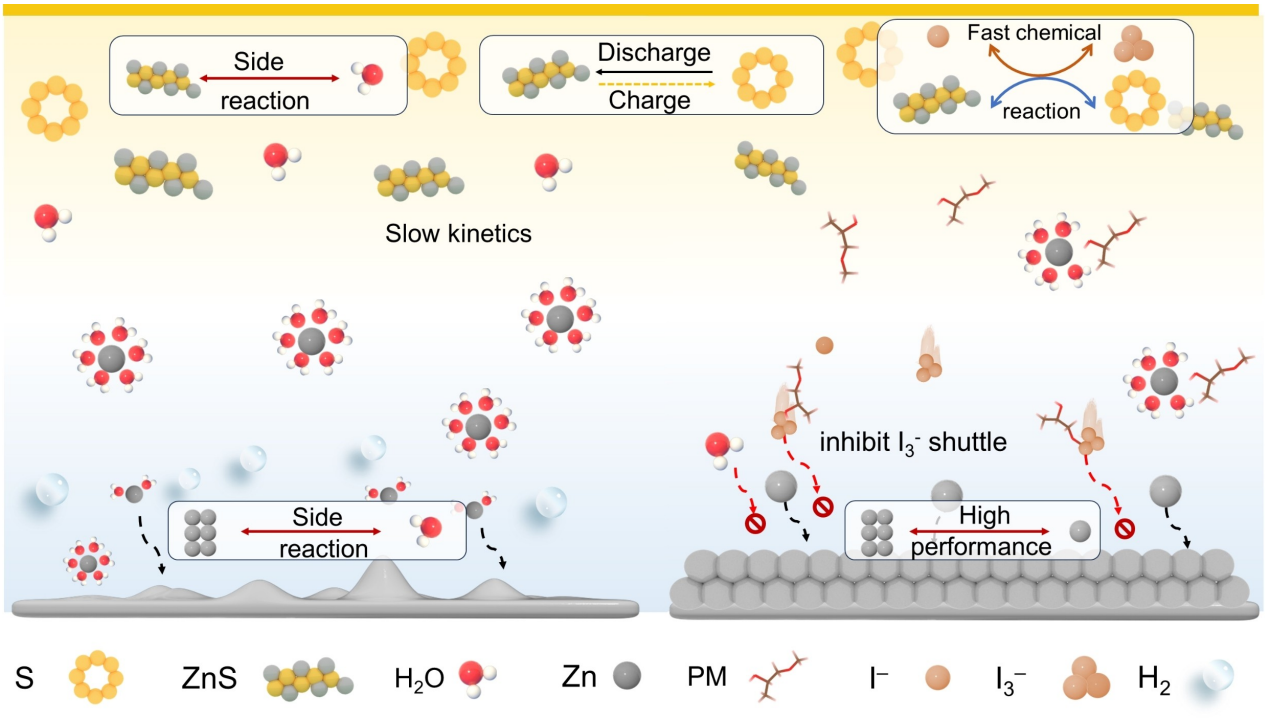

Scheme 1. Schematic illustration of aqueous Zn-S batteries in different electrolyte configurations: Zn–S batteries with 1 M $Zn(OTF)_2$ in water electrolyte (left) and Zn–S batteries with 1 M $Zn(OTF)_2$ in a PM/H_2O mixture with ZnI_2 additive (right). The presence of PM improves the interface stability of sulfur cathode and zinc anode, reducing dendrite growth and enhancing the longevity of the battery. The presence of ZnI_2 improves the reversibility of sulfur cathode. The PM co-solvent and ZnI_2 facilitate better redox reactions at the sulfur cathode, leading to higher capacity and energy density.

for the redox reaction of I^-/I_3^-, ultimately enhancing the kinetics of the sulfur cathode reaction. In addition, the presence of terminal -OH groups in PM can effectively regulate the solvation structure and hydrogen bonding network of Zn^{2+}, accelerating the zinc ion transport and suppressing by-products of the sulfur conversion process.

The stability of the negative electrode is also crucial for long life batteries. The presence of PM can change the coordination environment of water molecules as well as the concentration of zinc ions on the anode side of the zinc anode, maintaining the stability of the zinc negative electrode (Scheme 1). Due to the optimized electrolyte design, zinc-sulfur batteries achieved a high capacity of 1,456 mAh g^{-1} at 0.2 A g^{-1} when PM was accounted for 60 % of the overall solvent volume. Meanwhile, the assembled Zn||Cu half-cell maintained a coulombic efficiency of 98.95 % after 1200 cycles. In addition, the optimized electrolyte enabled zinc-sulfur batteries to achieve a high energy density of 471.8 Wh kg^{-1}, while ensuring the inherent safety of an aqueous electrolyte by being non-flammable, low-cost, and non-toxic.

Results

2.1 Tuning the Electrolyte Structure

Designing an effective electrolyte involves ensuring the reversibility of zinc deposition and stripping, along with facilitating rapid sulfur redox transformation. Zinc trifluoromethanesulfonate ($Zn(OTF)_2$) was fixed at a concentration of 1 M and dissolved in a mixture of PM and H_2O at various volume ratios (1:2; 1:1; 3:2, 2:1). The effective utilization of charge during the charge/discharge cycle of batteries was investigated by the Coulombic efficiency (Figure S1). In addition, the deposition and stripping phases of zinc anodes at various PM:H_2O volume ratios were analyzed via SEM (Figure S2). The results reveal that the zinc anode exhibits a uniform and smooth surface during plating and stripping when the PM:H_2O volume ratio is 3:2. At this ratio, the performance of Zn–S cells remains optimal. As shown in Figure S3, the Z/W/PM/I electrolyte demonstrates excellent rate performance with the addition of 0.05 M ZnI_2.

To evaluate the safety level of the developed electrolyte (PM to H_2O volume ratio of 3:2), a flammability test was conducted. It shows digital photographs captured during the flammability test in which commercial GF separators were immersed in various electrolytes (Figure S4). The results demonstrated that the electrolyte with 60 % PM was within safe levels. In addition, the ionic conductivity of the electrolyte was tested for different PM concentrations. The results show that the ionic conductivity is 9 mS cm^{-1} when the PM volume fraction reaches 60 %. This indicates that even with the addition of PM, the electrolyte maintains sufficient ionic conductivity to ensure efficient ion transfer for Zn–S cell operation (Figure S5). The mechanism by which alcohol ether solvent molecules inhibit the activity of water molecules was investigated using NMR spectroscopy, Raman scattering, and FTIR tests. The ^1H NMR spectra of the electrolyte was shifted upfield after the addition of PM (Figure 1a), indicating an increase in the proportion of solvent molecules involved in solvation shells and a weakening of water interactions. This is consistent with the Raman test results (Figure S6).[14] Compared with the conventional Z/W ($Zn(OTF)_2/H_2O$) electrolyte, a blue shift of the O–H stretching peak was observed in the electrolyte with PM, indicating that PM disrupts the pristine hydrogen bonding network and forms intermolecular hydrogen bonds between isolated water molecules and lone pairs of electrons on the oxygen atoms in PM.[15] The introduction of iodine does not change the position of the hydrogen bond peak, indicating that iodide ions are not involved in the first solvation shell, consistent with molecular dynamics (MD) simulation results. Infrared test results further confirmed the disruption of the hydrogen bonding network. In the FTIR spectra, the peak ascribed to the O–H bending vibration (3000-3500 cm^{-1}, 1600–1700 cm^{-1}) in the Z/W/PM ($Zn(OTF)_2$/Water/PM) electrolyte shifts to a higher wavenumber compared to the Z/W electrolyte (Figure 1b and Figure S7). As the PM concentration increases, the peak of O–H in H_2O weakens and shows a blue shift, which indicates that the H-bonding interactions between the H_2O molecules are weakened (Figure S8). Additionally, the red shift of the OTF^-stretching vibration peak ($\approx$1027 cm^{-1}) after the addition of PM, observed in the FTIR spectra, indicates that the interaction between Zn^{2+} and OTF^- in the Z/W/PM electrolyte is enhanced, effectively altering the solvated structure of Zn^{2+}(Figure 1c).[16]

The solvated structure of Zn^{2+} was theoretically analyzed using MD simulations (Figure 1d-h). In different electrolyte systems, Zn^{2+} is preferentially coordinated to six molecules in the first solvation shell, but the structure varies in different electrolytes. Radial distribution functions (RDFs) and coordination numbers were analyzed for Z/W/I ($Zn(OTF)_2/H_2O/ZnI_2$) and Z/W/PM/I ($Zn(OTF)_2/H_2O$/PM/ZnI_2) electrolytes. In the Z/W/I electrolyte, a sharp peak of Zn^{2+} (H_2O)-O was observed at a distance of about 2.1 Å from Zn^{2+}, with a simulated average coordination number of 5.5, indicating that the Zn^{2+} solvation shell is mainly $Zn[H_2O]_6^{2+}$ (Figure S9 and S10). In the Z/W/PM/I electrolyte, the average coordination number of Zn^{2+}(H_2O)-O is reduced to 4.3, the OTF^- and PM appear in the Zn^{2+} solvation structure due to their strong coordination ability (Zn^{2+} can attract the lone pair of electrons on O in PM to form PM-Zn^{2+} coordination via Lewis acid-base interactions).[17] In both electrolytes, the added iodine source is in the second solvation shell layer of the zinc ions, which indicating minimal interaction between iodine ions and zinc ions. This structure reduces the contact of iodine ions with the zinc negative electrode, avoiding corrosion effects.

2.2 Stability and Reversibility of Zn Anode

Anti-corrosion performance is a critical parameter for evaluating the stability and reversibility of zinc plating and stripping. The corrosion current density at the zinc anode in the Z/W/PM/I electrolyte (0.13 mA cm^{-2}) is much smaller

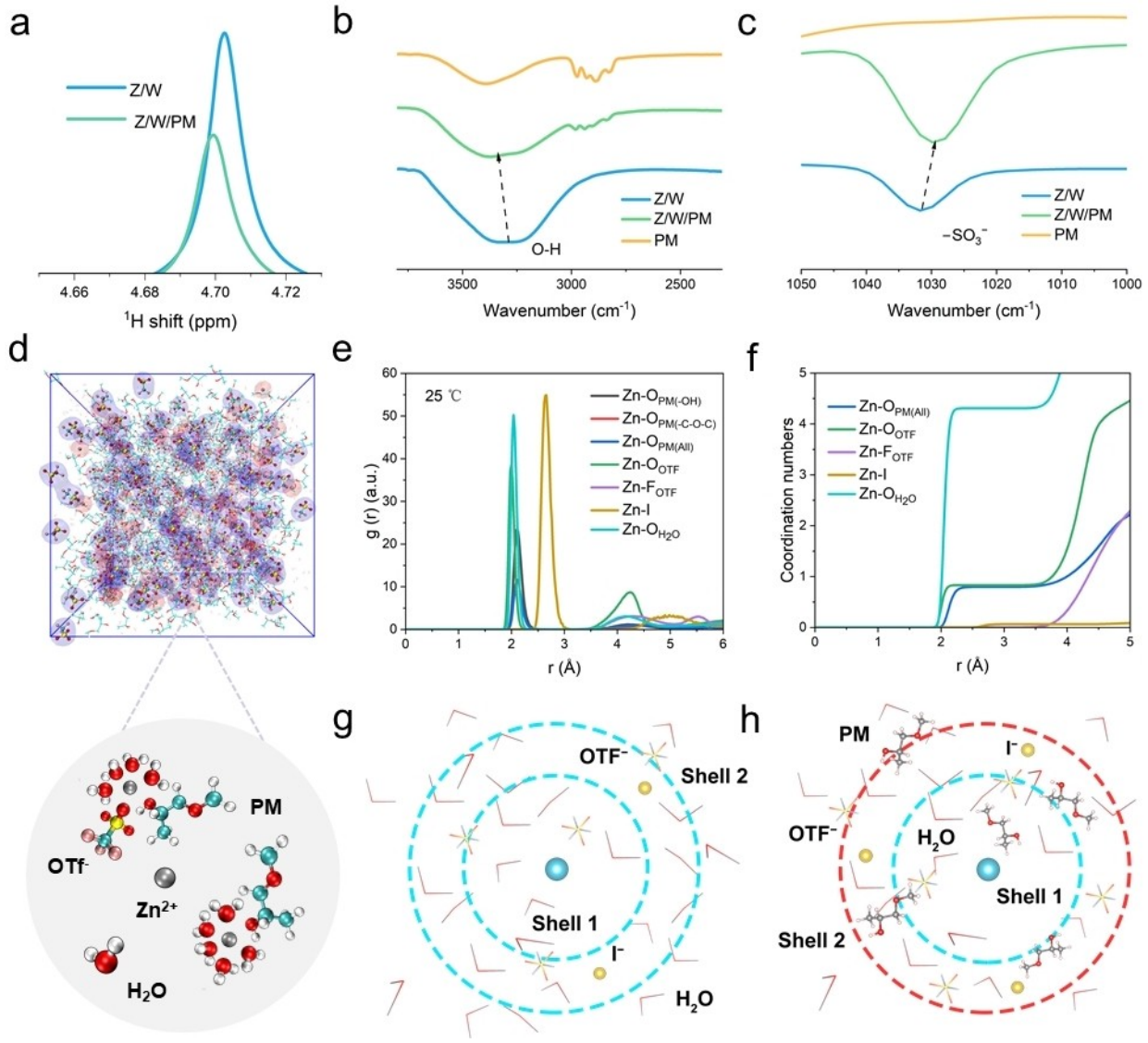

Figure 1. Molecular dynamics simulation of the local solvation environment. (a) ^{1}H nuclear magnetic resonance (NMR) spectra of Z/W and Z/W/PM electrolytes. (b-c) Fourier transform infrared (FTIR) spectra of the PM, Z/W and Z/W/PM electrolytes. (d) Snapshot from MD simulations of Zn^{2+} solvation structures in the Z/W/PM/I electrolyte. (e-f) Radical distribution functions (RDFs) and coordination number distribution functions obtained from MD simulations for Zn^{2+} solvation structures in the Z/W/PM/I electrolyte. (g-h) Schematic structures of Zn^{2+} solvation in Z/W/I and Z/W/PM/I electrolytes.

than that in the Z/W/I electrolyte (1.13 mA cm^{-2}) (Figure 2a). It indicates that zinc corrosion is more difficult with the introduction of PM. Corrosion inhibition is essential for preventing zinc dendrite growth because the corrosion reaction can induce an irregular distribution of the electric field and ion concentration at the zinc deposition interface.[18] Similarly, the increase in hydrogen evolution reaction (HER) overpotential implies that PM inhibits the HER side reaction (Figure 2b). The oxygen evolution reaction (OER) is also suppressed with the onset potential increasing from 2.51 to 2.61 V (Figure 2c). The Z/W/PM/I electrolyte offers a wider electrochemical stabilization window (ESW) of 2.67 V compared to 2.56 V for the Z/W/I electrolytes, assisting to minimize side reactions from electrolyte decomposition.

The diffusion behavior of zinc ions in different electrolytes was investigated using chronoamperometric (CA) tests (Figure 2d). The current densities of both electrolyte systems increased rapidly in the initial 70 s, indicating a disordered two-dimensional diffusion process in the early stage. Typically, zinc ions adsorbed on the surface of a bare zinc foil gain electrons and turn into zinc atoms, which then freely migrate to nearby tiny protrusions (e.g., zinc nucleus) with high specific surface energies, eventually forming larger dendrites.[17] In contrast, the homogeneous diffusion behavior in the electrolyte system containing PM leads to a gradual stabilization of the current, ensuring uniform distribution of nucleation sites for subsequent zinc flat deposition. To elucidate the role of PM in inhibiting zinc anode side reactions, the adsorption energies of H_2O and

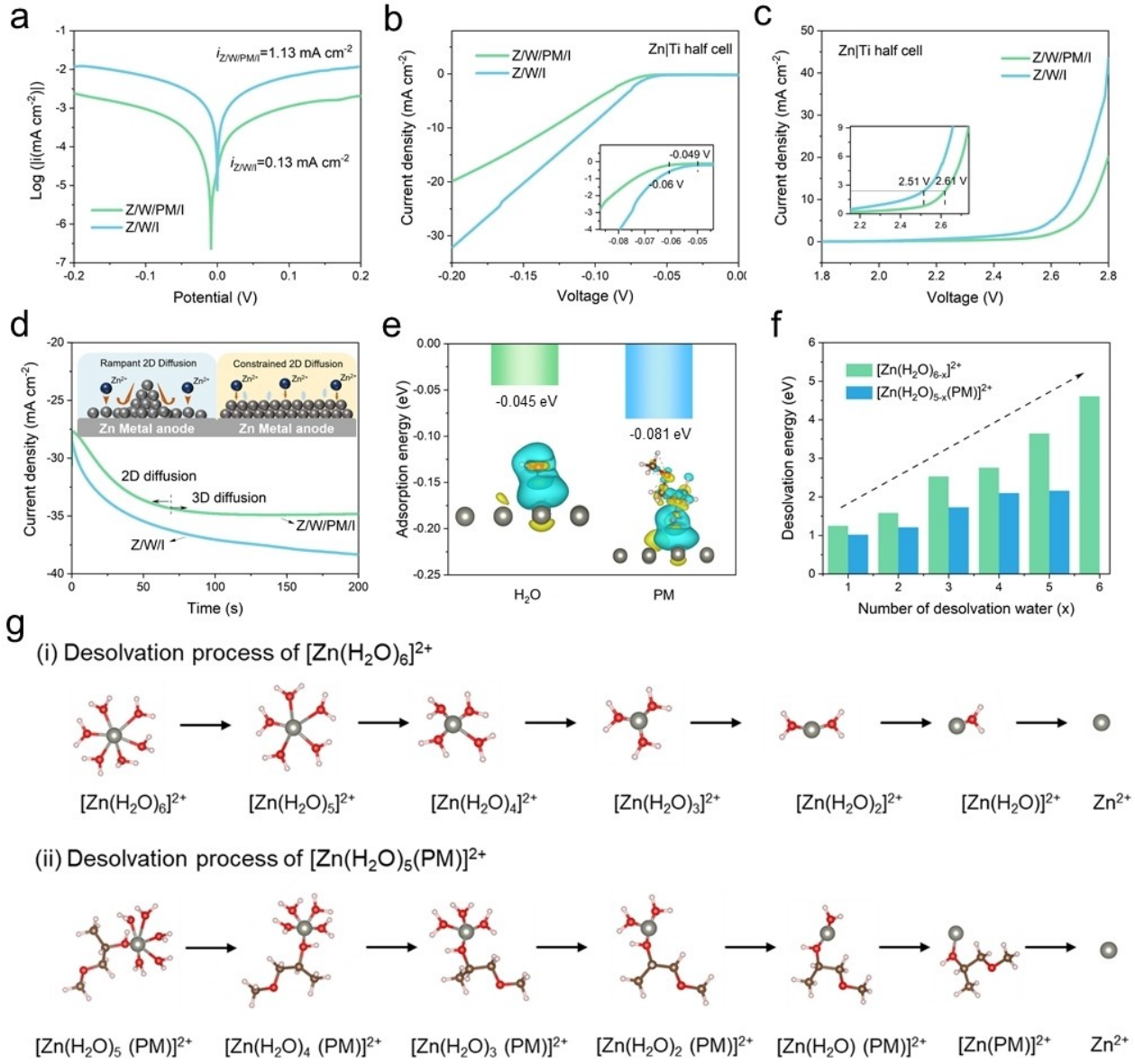

Figure 2. Kinetics and stability of zinc anodes. (a) Tafel polarization curves of Zn anodes in Z/W/I and Z/W/PM/I electrolytes. (b-c) Linear sweep voltammetry (LSV) curves to determine the electrochemical stability potential window at a scan rate of 2 mV s^{-1} in Z/W/I and Z/W/PM/I electrolytes. (d) Chronoamperometric (CA) curves of Zn||Zn cells at a constant overpotential of −150 mV in Z/W/I and Z/W/PM/I electrolytes. The inset shows schematic diagrams of two forms of zinc deposition. (e) The adsorption energy of H_2O and PM on the zinc anode surface. (f) The desolvation energies of $[Zn(H_2O)_{6\text{-}x}]^{2+}$ (x = 1-6) and $[Zn(H_2O)_{5\text{-}x}(PM)]^{2+}$ (x = 1-5). (g) Comparison of energy barriers during the step-by-step desolvation process of $[Zn(H_2O)_{6\text{-}x}]^{2+}$ (x = 1-6) and $[Zn(H_2O)_{5\text{-}x}(PM)]^{2+}$ (x = 1-5). The gray, red, white, and brown balls represent zinc, oxygen, and carbon atom, respectively.

PM on bare Zn surfaces were calculated (Figure 2e). The adsorption energy of H_2O molecules on the bare zinc surface is −0.045 eV, whereas the adsorption energy of PM molecules is −0.081 eV. This suggests that the preferential adsorption of PM on the bare zinc surface reduces problems such as corrosion and hydrogen precipitation due to the high activity of water and dissolved oxygen.[19] Density functional theory (DFT) was used to calculate the PM-enhanced desolvation and its effect on Zn^{2+} diffusion kinetics (Figure 2f and g). The dissociation of the solvated structure in the PM-added electrolyte requires less energy compared to the conventional Z/W/I electrolyte. Additionally, the energy required to remove a water molecule for $[Zn(H_2O)_{5\text{-}x}(PM)]^{2+}$ (x = 1-5) ranges from 1.02 to 2.16 eV, which is much lower than the energy needed to remove a water molecule from $[Zn(H_2O)_{6\text{-}x}]^{2+}$ (x = 1-6), ranging from 1.25 to 4.61 eV. This is mainly attributed to the hydroxyl functional group, which can coordinate individually to the central Zn^{2+} ion, significantly lowering the energy barrier for the desolvation process. Consequently, $[Zn(H_2O)_{5\text{-}x}(PM)]^{2+}$ (x = 1-5) clusters can easily desolvate water in the

ligand structure after solvation remodeling, which improves transport kinetics and interfacial compatibility.

2.3 Electrochemical Stability of Zn Anode

In addition to the electrolyte stability, the reversibility of zinc anode is a crucial for achieving high energy density and good electrochemical performance. The reversibility of zinc plating/stripping in different electrolytes was studied using Zn||Zn symmetric cells and Zn||Cu cells. Zn||Cu cells were tested at a current density of 0.5 mA cm^{-2} for more than 10 cycles to evaluate the plating/stripping ability of both electrolytes (Figure 3a). Compared to the Z/W/I electrolyte, which has a low coulombic efficiency (CE) of 77.43 %, the Z/W/PM/I electrolyte exhibits a higher average CE of 86.72 %. This improvement is attributed to the enhanced uniformity of zinc deposition, facilitating a more favorable zinc ion plating and stripping process. Furthermore, the PM-treated electrolyte was able to run smoothly for 1200 cycles at a current density of 1 mA cm^{-2} with an average CE value of more than 98.95 %. In stark contrast, the Z/W/I electrolyte experienced a sudden drop in CE due to the continued formation of dead zinc, leading to a short circuit (Figure 3b). Voltage profiles of different cycles showed that the overpotential could be stabilized even during cycling at a high current density (3 mA cm^{-2}) (Figure S11). These results confirm that the addition of PM formed an ultra-stable zinc/electrolyte interface.

Adding PM to the electrolyte also facilitates the long cycle performance of Zn||Zn symmetric batteries. At a current density of 1 mA cm^{-2} with a capacity of 1 mAh cm^{-2},

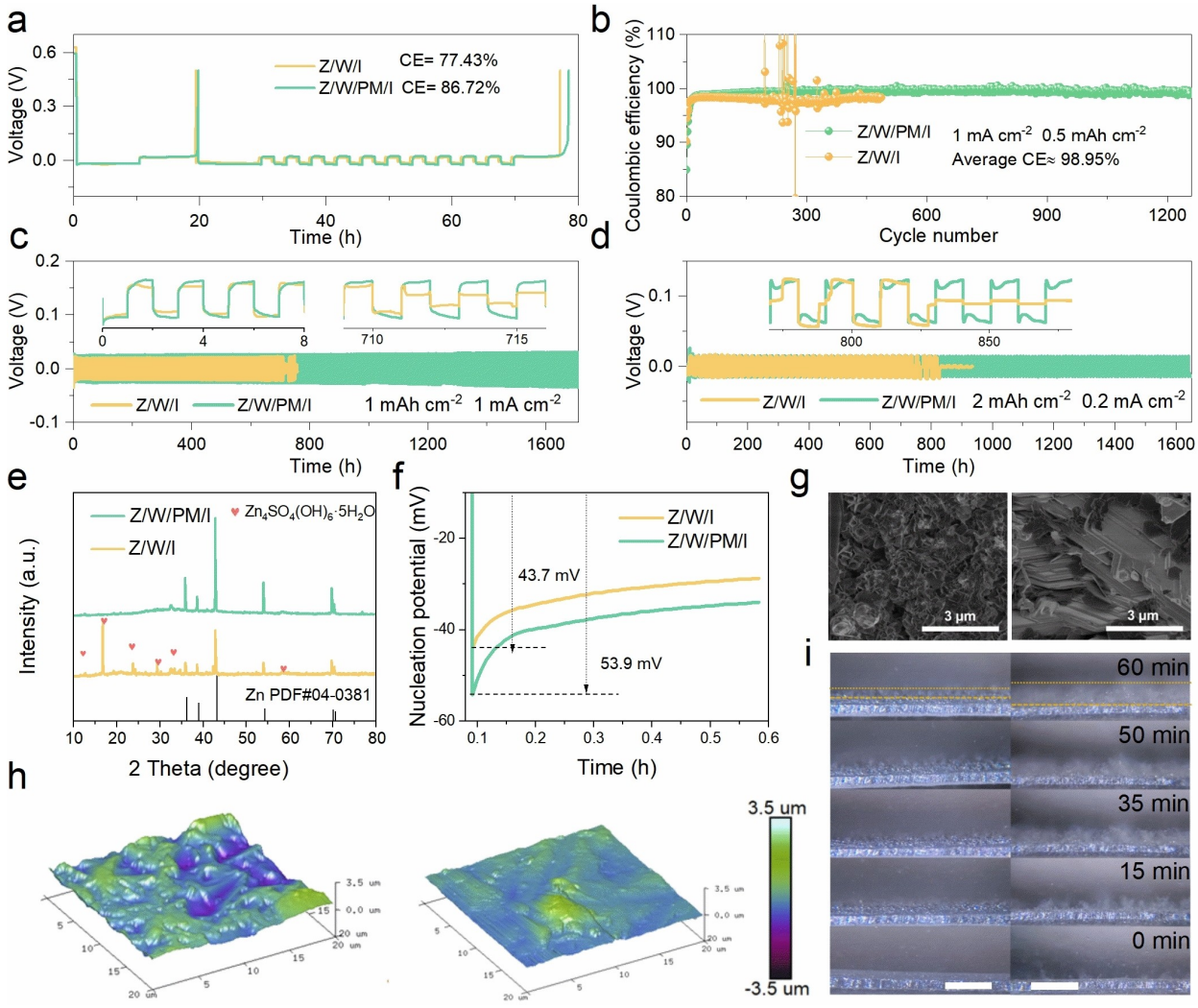

Figure 3. Electrochemical performance of the Zn anode in (a)symmetric cells. (a-b) Measured Coulombic efficiency (CE) of Zn||Cu cells at 1 mA cm^{-2} in Z/W/I and Z/W/PM/I electrolytes. (c) Cycling performances of Zn||Zn symmetric cells in Z/W/I and Z/W/PM/I electrolytes at 1 mA cm^{-2} with a capacity 1 mAh cm^{-2}. (d) Cycling performances at 0.2 mA cm^{-2} with a capacity 2 mAh cm^{-2}. (e) XRD patterns of the Zn anode after 20 cycles in Z/W/I and Z/W/PM/I electrolytes at 1 mA cm^{-2} and 1 mAh cm^{-2}. (f) Initial zinc nucleation overpotential in Z/W/I and Z/W/PM/I electrolytes. (g) SEM images of Zn||Cu cells at 1 mA cm^{-2} in Z/W/I and Z/W/PM/I electrolytes. (h) AFM images of the surface of Zn anodes in Z/W/I and Z/W/PM/I electrolytes. (i) In situ optical visualization of Zn deposition in Z/W/I electrolyte (right) and Z/W/PM/I (left) electrolyte (left), scale bar: 50 μm.

the Z/W/PM/I electrolyte achieves a stable cycling performance of 1650 h. In contrast, cells without PM failed after about 700 h of cycling (Figure 3c). Even under deep charging and discharging conditions (0.2 mA cm^{-2}, 2mAh cm^{-2}), the electrolyte with PM can run smoothly for more than 1600 hours (Figure 3d). XRD analysis was used to determine the surface composition after 20 cycles (Figure 3e). The bare zinc surface has distinct characteristic peaks at 16.15° and 24.27°, attributed to the by-product $Zn_4SO_4(OH)_6{\cdot}x\ H_2O$ (PDF#39-0688). Notably, these peaks are less pronounced in the PM-added electrolyte, suggesting that PM effectively avoids the generation of by-products.

The nucleation overpotential of Zn||Ti asymmetric cells further analyzed the deposition behavior of Zn (Figure 3f). During zinc deposition in the Z/W/PM/I electrolyte system, the initial nucleation overpotential is 53.9 mV, a measure of the energy barrier that must be overcome to form stable nuclei. This value is significantly higher than the corresponding overpotential of 10.2 mV observed in the Z/W/I electrolyte. This higher energy requirement promotes more uniform zinc deposition in the Z/W/PM/I electrolyte by applying a stronger driving force during the critical initial nucleation phase.[20] Figure 3g illustrates the morphology of the initial zinc deposition of Zn||Cu cells at 1 mA cm^{-2} and 1 mAh cm^{-2}. In the Z/W/I electrolyte, the zinc anode surface exhibits a loose porous stacking structure with random dendrites. Conversely, with the addition of PM, a smooth, dense zinc deposition layer with evident laminar epitaxial growth is observed. The enhanced Zn (002) peak confirms that zinc ions prefer to be deposited along the (002) crystal surface (Figure S12), suggesting that PM molecules at the interface significantly modulate the orientation of zinc deposition during the plating/stripping process.

Scanning electron microscopy (SEM) and atomic force microscope (AFM) were used to observe the zinc surfaces of Zn||Zn symmetric cells after 50 cycles in different electrolytes at 1 mA cm^{-2} and 1 mAh cm^{-2} (Figure 3h and Figure S13). In the Z/W/PM/I electrolyte, the zinc surfaces remained flat and smooth (surface roughness of 154 nm), whereas in the Z/W/I electrolyte, rampant dendrite growth occurred on the zinc surface, accompanied by severe side reactions that led to the formation of aggregated mossy zinc deposits and the generation of electrochemically inactive "dead zinc" (surface roughness of 219 nm). Direct evidence of PM's ability to inhibit side reactions and modulate zinc plating/stripping was obtained through *in situ* optical visualization of the zinc deposition process. Figure 3i illustrates the process variation of zinc deposition in one hour at a current density of 10 mA cm^{-2} for both electrolytes. In the electrolyte without PM, the zinc evolves into a severely fluffy dendritic form within 15 minutes due to uneven zinc deposition, and the dendritic phenomenon intensifies over time. In contrast, the PM-added electrolyte showed uniform and dense zinc deposits during the one-hour deposition process. These observations indicate that PM effectively protects the zinc electrode from side reactions while promoting the orderly deposition of zinc and thereby inhibiting the growth of dendrites.

2.4 Reaction Mechanism of Aqueous Zinc-Sulfur Batteries

To investigate the effect of different electrolytes on the interfacial kinetics and stability of the sulfur cathode and zinc anode, *in situ* electrochemical impedance spectroscopy (EIS) was used to study the changes in electrochemical reactions during the first cycle of the zinc-sulfur cell (Figure 4a). The EIS plots of the cells in both electrolytes exhibit analogous tendencies. Specifically, the first discharge plateau (0.4 V) and the initial charge plateau (1.3 V) manifest diminished charge transfer resistances, signifying expeditious redox kinetics. Conversely, larger charge transfer resistances at lower voltages compared to higher voltages indicates hindered kinetics. This is due to the fact that the cathode structure changes with the gradual deposition of poorly ion-conducting ZnS during low-voltage discharges, which may create new pore structures and lead to the loss of electrode blocking behavior.[21]

Unfortunately, in the EIS results, it is difficult to discern the changes in each process at the electrode-electrolyte interface and the contribution to the overall resistance without knowing the reaction mechanism by which the cell operates. Therefore, we employed distribution of relaxation time (DRT) analysis to probe the changes occurring at the interface. Different electrochemical processes are distinguished and separated by means of different time constants (τ) that represent the intrinsic properties of each process (grain boundaries, volume and ionic conduction at the contact interface) over a wide frequency range, which is tightly correlated with the performance of the cell (Fig. 4b-e). The electrochemical reaction process is divided into three parts $\tau1$ process ($\tau1 > 1$ s), $\tau2$ process ($\tau2 \sim 0.01-1$ s), and $\tau3$ process ($\tau3 <$ 0.01 s) corresponding to the mass transport of the electrolyte phase in the electrolyte-filled pores, the charge-transfer reaction, and the ionic transport in the SEI layer, respectively.

As shown in Figure 4b and c, the $\tau1$ of the electrolyte without PM is significantly stronger than that of the Z/W/PM/I electrolyte for the first discharge to 0.4 V (the first measurement of the EIS), suggesting that the wettability of PM to the sulfur cathode accelerates the transport of ions to the active material. Moreover, in addition to the changes in the discharge and charging plateaus, it can be noticed that the peak of $\tau1$ is stronger in the low voltage state compared to the high-voltage state, indicating that the continuous surface adsorption and insertion of zinc ions leads to a delay in the transport kinetics.[22] At high voltages, the transport of zinc ions within the electrodes is accelerated following a continuous process of adsorption and dissociation.

In the enlarged plot (Figure 4d), the peak of $\tau2$ shows a decreasing-increasing-decreasing trend during charging and discharging processes, whereas no such pattern is observed in the Z/W/I electrolyte (Figure 4e). The charge transfer resistance becomes smaller during charging at high voltage potentials, which suggests that PM can lower the decomposition energy barrier of ZnS while promoting

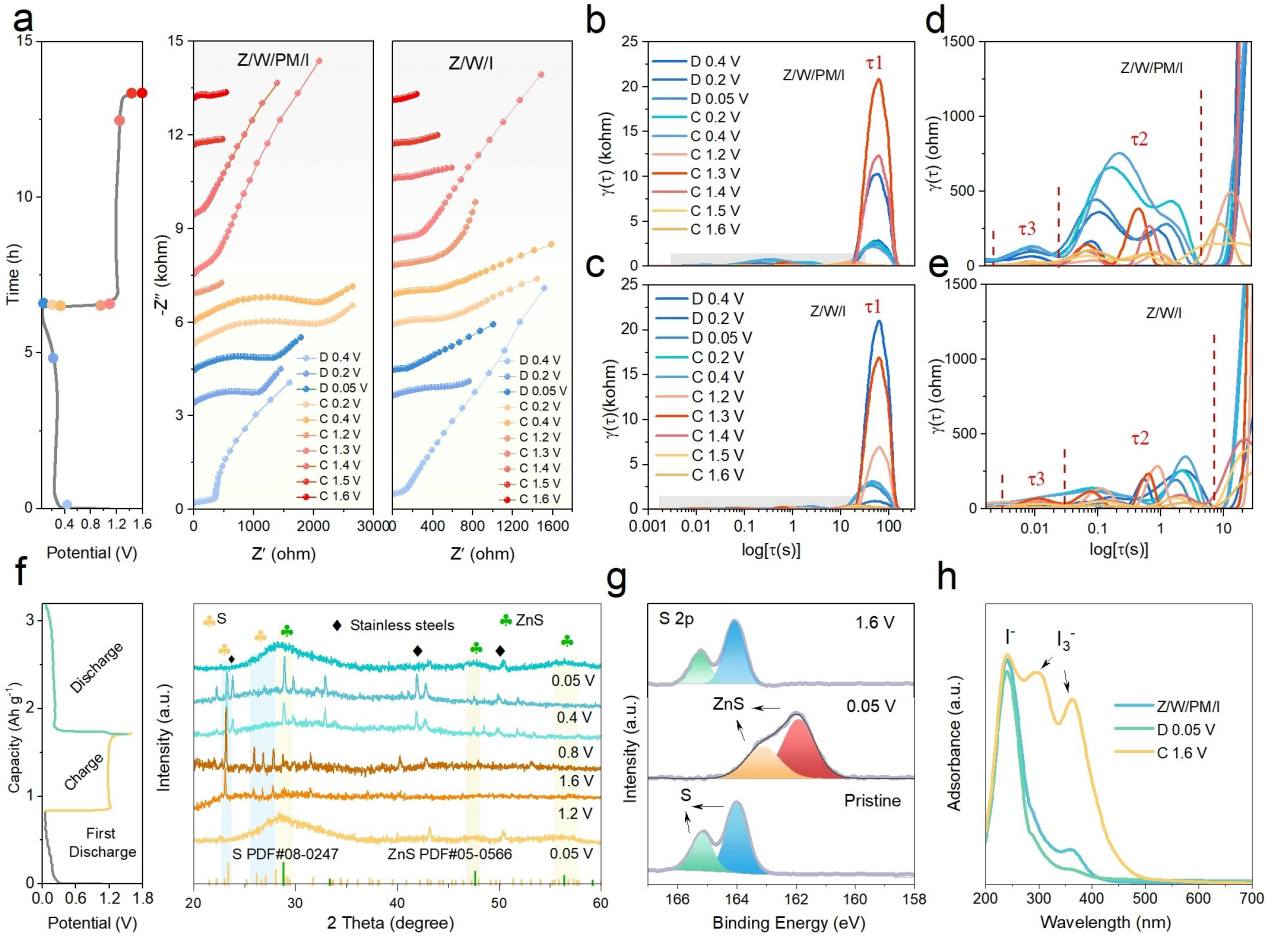

Figure 4. Mechanism elucidation of the synergy of PM and ZnI_2. (a) Electrochemical impedance spectroscopy (EIS) spectra of Zn–S cells in the Z/W/PM/I electrolyte. (b-e) DRT analysis of the EIS results at different potentials in Z/W/PM/I and Z/W/I electrolytes. (f) *Ex situ* XRD patterns during the discharge and charge processes. (g) *Ex situ* S 2p XPS at the labeled states. (h) *Ex situ* UV-vis absorption spectra of changes in electrolyte at the labeled states.

the removal of water molecules from the solvated structure of zinc ions. For the τ3 peak, if we assume that the compositions and resistances of the SEI layer and the resistance across the SEI remain constant, τ3 can be expressed as the thickness of the SEI. Therefore, the increase of τ3 indicates the growth process of SEI, showing continuous growth to stabilization from the initial discharge process to the charging process, thereby building a reliable zinc anode SEI and enhancing stability. In contrast, the unstable formation of SEI in the Z/W/I electrolyte suggests that the mechanical properties of SEI will be challenged as cycling proceeds. The role of the iodine source in the electrolyte was analyzed by DRT (Figure S14). Overall, the total impedance of the zinc-sulfur batteries in the Z/W electrolyte is very high, indicating severely hindered kinetics. This demonstrates that the iodine source improves the kinetics of the solid-solid transition reaction during charging and discharging. In addition, the τ3 process shows that SEI growth is not stabilized, proving that PM plays an important role in SEI formation and the inhibition of by-products. To further investigate the role of PM, the electrolyte interface chemistry was analyzed using Ar^+ sputtering combined with X-ray photoelectron spectroscopy (XPS) (Figure S15). In addition to the fluorocarbon signals from OTF−, the XPS results reveal the presence of C–O (285.4 eV), C–C/C–H (284.7 eV), and $ZnCO_3$ (288.3 eV), which are attributed to the electrochemical decomposition and surface adsorption of PM. The promotion of anion decomposition by PM is further evidenced in the F 1s spectra. In the Z/W/PM/I electrolyte, the ratio of inorganic to organic fluorine increases with etching depth. Specifically, the C–F bond signal at 688.5 eV arises from anion adsorption, while the Zn–F bond at 684.4 eV indicates anion decomposition. At the same sputtering depth, the ZnF_2 content in the Z/W/PM/I electrolyte is significantly higher than in the Z/W/I electrolyte, confirming that PM facilitates anion decomposition (Figure S16). In the Z/W/PM/I electrolyte, the dipole moment induced by the hydroxyl groups in PM enhances electron transfer from the zinc anode to the electrolyte, leading to the formation of a multilayered SEI. This ZnF_2-rich interface serves as a protective layer, enabling highly reversible zinc anode performance.

The conversion reaction mechanism of the zinc-sulfur battery was characterized using a ex situ XRD, measured by discharging the battery from the open circuit voltage (1.13 V) at constant current to 0.05 V and then charging the battery at constant current to 1.6 V. As shown in Figure 4f, diffraction peaks appeared at 28.54°, 47.57°, and 56.36° at the initial discharge to 0.05 V, corresponding to the characteristic peak of ZnS.[23] When charging from 0.05 V to 1.6 V, the sulfur peaks (23.1°, 25.95°, 27.84°) were gradually enhanced and the crystallinity increased. When discharging to 0.05 V again, the gradual disappearance of the sulfur peaks is accompanied by the obviousness of the ZnS peaks, confirming the reversible transformation of sulfur and zinc sulfide during the charging and discharging process of the battery with no observed polysulfides.

Changes in the sulfur cathode was further investigated by XPS (Figure 4g). The unreacted initial sulfur cathode electrode sheet showed double peaks at binding energy (BE) of 164 and 165.1 eV, corresponding to the sulfur peaks. At complete discharge to 0.05 V, new peaks appeared at 161.9 and 163.1 eV due to the generation of ZnS, at which point the peaks of S_8 completely disappeared. When charged to 1.6 V, the peak of sulfur reappeared and the peak of ZnS decreased, confirming the reversible conversion between zinc sulfide and sulfur during cycling. The BE changes in the region of I 3d during charging and discharging were also investigated by XPS (Figure S17). At the fully discharged state, the sulfur cathode showed the peaks of I^- at 618.6 eV and 630 eV.[24] When fully charged, the peaks of I^- weakened considerably and new BE peaks of I_3^- appeared simultaneously (620, 631.5 eV), which aligns with the results of UV (Figure 4h). Changes of iodide ions in the electrolyte were investigated by UV-visible spectroscopy in fully charged and fully discharged states. In the fully discharged (0.05 V) state, the signal of I_3^- almost disappeared, and a new peak of I_3^- appeared with an enhanced original peak in the fully charged state (1.6 V),[25] which confirms that iodine reaction further catalyzes the conversion kinetics of the sulfur cathode during charging and discharging with PM assistance. Compared to the Z/W/I electrolyte, the signal of I^- in the Z/W/PM/I electrolyte was greatly weakened, while the signal of I_3^- is enhanced, indicated that the electronegative groups in PM are capable of triggering some of the I^- to I_3^- transitions during electrolyte preparation (Figure S18). These test characterization results reveal the electrochemical behavior and effects of iodine source introduction and PM co-solvent addition on catalytic sulfur cathodes in zinc-sulfur batteries.

2.5 Electrochemical Performance of Aqueous Zn-S Batteries

The sulfur-activated material was bound to commercial carbon (Figure S19) through a typical melt diffusion process. A sulfur content of ~70 % was confirmed by thermogravimetric analysis (TGA) (Figure S20). To demonstrate the synergistic effect of the iodine source and PM on the sulfur positive electrode, the CV curves of various electrolytes were tested (Figure 5a). A pair of redox peaks was observed for all four electrolytes at 0.2 $mV s^{-1}$, corresponding to the reduction of S_8 and oxidation of ZnS. Notably, a pair of redox peaks appeared in the electrolytes with the iodine source, indicating its catalytic effect on the cathode. The reduction peaks at approximately 1.2 V can be attributed to the electrochemical control of iodine species, as verified in Figure S21.

Comparing the electrochemical behaviors of Z/W/I, Z/W/PM/I, Z/W, and Z/W/PM electrolytes using CV curves in zinc-sulfur batteries, it was found that the absence of PM addition led to substantial increases in polarization and current density, attributed to water-induced parasitic reactions and slow kinetics. In contrast, the introduction of PM reduced polarization and presented stable reduction peaks, indicating good electrochemical performance for sulfur conversion. Additionally, the CV curves of the Z/W/PM/I electrolyte exhibited well-defined oxidation and reduction peaks across various scan rates, indicating good reversibility of the redox couple zinc storage process (Figure S22). To evaluate cycling stability, GCD and CV curves were recorded for the first four cycles in the Z/W/PM/I electrolyte. The GCD curves exhibit well-defined charge/discharge plateaus, while the CV curves show stable redox peaks (Figure S23).

GCD tests with different electrolytes were conducted at a current density of 0.2 $A g^{-1}$ to evaluate the improvements in electrochemical performance due to the synergistic effects of PM and ZnI_2 (Figure 5b). The results demonstrate that the Z/W/PM/I electrolyte reduces the charging voltage plateau and increases the discharge plateau compared to Z/W/I and Z/W electrolytes. Notably, the Z/W/I and Z/W systems exhibit greater voltage hysteresis, indicating higher polarization. These findings highlight the role of PM in improving the reactivity of sulfur (S) and zinc sulfide (ZnS) and enhancing the electrode reaction rate. To further evaluate the catalytic kinetic properties of the iodine source in promoting ZnS nucleation, the ZnS nucleation response time (solid-solid conversion ratio) was tested after the first cycle and after eight cycles using an electrostatic potential discharge test (Figure 5c and Figure S24). The Z/W electrolyte releasesed a capacity of 1,489 $mAh g^{-1}$ in the initial cycle but only 115 $mAh g^{-1}$ after eight cycles. In contrast, the Z/W/I electrolyte with the iodine source released 1508 $mAh g^{-1}$ in the first cycle and retained 1203 $mAh g^{-1}$ after eight cycles, demonstrating the excellent catalytic effect of the iodine source on the sulfur cathode.

To quantitatively assess the impact of the iodine source on the migration of Zn^{2+} ions, a Zn–S cell configuration was employed. The activation energy (Ea) associated with the interfacial diffusion barrier for zinc ions in the Z/W/PM and Z/W/PM/I electrolyte systems was evaluated by analyzing the impedance response over the temperature range of 25–50 °C. The Arrhenius equation was utilized to extract the activation energy from the temperature-dependent impedance data, elucidating the

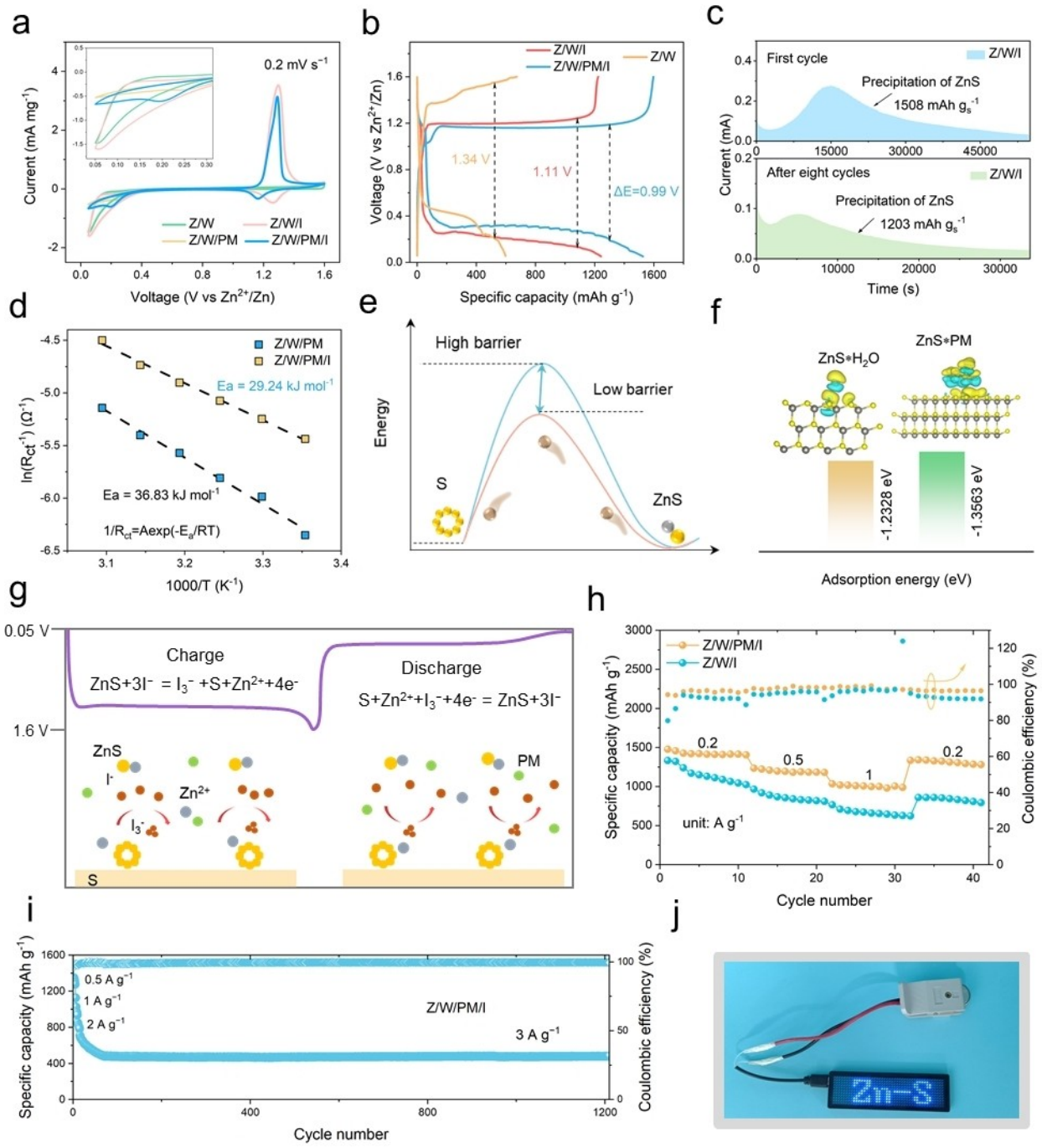

Figure 5. Electrochemical performance of full cells. (a) CV curves of Zn–S cells in Z/W/PM/I, Z/W/I, Z/W, and Z/W/PM electrolytes. (b) GCD curves of Zn–S cells in Z/W, Z/W/PM/I, and Z/W/I electrolytes. (c) Potentiostatic discharge profiles of ZnS nucleation at 0.3 V in Z/W/I and Z/W/PM/I electrolyte. (d) Comparison of activation energies of Z/W/PM/I and Z/W/I electrolytes. (e) Conversion energy barriers for S and ZnS in Z/W/PM/I and Z/W/I electrolytes. (f) Calculated adsorption energy of ZnS*H_2O and ZnS*PM. (g) Schematic diagrams of the discharge and charge processes involving the iodine source and PM. (h) Rate performance of the Zn–S batteries in Z/W/I and Z/W/PM/I electrolytes. (i) Long-cycle performance of Zn–S cells in the Z/W/PM/I electrolyte at a current density of 3 A g^{-1}. (j) Digital image of two Zn–S coin cells connected in series powering an LED.

effect of iodine addition on the kinetics of zinc ion transport across the electrode-electrolyte interface.[26]

$$R_{ct}^{-1} = Ae^{\frac{-Ea}{RT}} \quad (1)$$

where R_{ct} is the charge transfer resistance, A is the frequency factor, R is the gas constant, and T is the absolute temperature. It was observed that the impedance decreases as the reaction kinetics increase with rising temperature (Figure 5d and Figure S25). The addition iodine source

resulted in a slight decrease of Ea from 36.83 to 29.24 kJ mol^{-1}, indicating its significant catalytic effect on the sulfur cathode.

The introduction of an iodine source reduces the energy barrier for the interconversion of S and ZnS (Figure 5e). Furthermore, PM effectively inhibited the generation of cathode by-products. SEM analysis revealed distinct morphological differences after five cycles, depending on the electrolyte composition. In the Z/W/PM/I electrolyte, the electrode sheets exhibited a dense and flat morphology. In contrast, the Z/W/I electrolyte without PM resulted in a rough morphology characterized by the formation of inhomogeneous nanosheets (Figure S26).

The interaction between the electrolyte solvent and the sulfur cathode component and was further analyzed using density flooding theory (DFT) calculations (Figure 5f).The adsorption energy of PM with ZnS is larger than that of water molecules and ZnS, indicating that PM molecules can be preferentially adsorbed on the surface of ZnS. It is worthwhile to note that a small amount of ZnS and water can lead to an irreversible sulfate generation under electrochemical conditions,[27] so that introducing the PM molecules can provide a stable electrolyte-interfacial phase and inhibit water-induced side reactions. Contact angle tests revealed that the introduction of PM into the electrolyte greatly increased the wettability of the sulfur cathode and ensured the effective electrochemical reaction at the electrode-electrolyte interface (Figure S27). These observations suggest that PM plays a crucial role in maintaining electrode integrity during cycling.

The effect of PM with the iodine source was further demonstrated with NMR tests. The increased ^{1}H chemical shift of the Z/W/PM/I electrolyte compared to the Z/W/PM electrolyte may be attributed to the coordination of the polar functional groups in PM with the I^- ion (Figure S28). The polar groups in PM, such as –OH and C–O–C, act as electron-donating entities, facilitating the evolution of I^- to I_3^-. This process results in the formation of I_3^- polar catalysts, which effectively promote the conversion kinetics at the sulfur cathode (Figure 5g).

Discharge process :

$$S + Zn^{2+} + I_3^- + 4e^- \rightarrow ZnS + 3I^- \quad (2)$$

Charge process :

$$ZnS + 3I^- \rightarrow I_3^- + S + Zn^{2+} + 4e^- \quad (3)$$

After understanding the working principle of PM and ZnI_2 in zinc-sulfur batteries, the cycling stability of Z/W/PM/I and Z/W/I electrolytes was tested at a current density of 0.5 A g^{-1}. The electrolyte without PM showed a rapid decay trend, while the PM containing electrolyte was relatively smooth cycling, proving that PM can inhibit the generation of by-products (Figure S29). Comparing the reversible performance of the two electrolytes at different current densities, the electrolyte with added ZnI_2 and PM provides 1410, 1196, 997, and 1340 mA h g^{-1} at current densities ranging from 0.2 to 1 A g^{-1}. In contrast, the capacity of electrolyte without PM decreased at each current density and was much lower than the initial state when the current density was restored to 0.2 A g^{-1} (Figure 5h).

To demonstrate the excellent effect of PM and ZnI_2 on zinc-sulfur cells, the cycling stability of four electrolytes was tested at a current density of 1 A g^{-1} (Figure S30). The Z/W/PM/I electrolyte enabled cells to maintain a capacity of 1000 mAh g^{-1} for 100 cycles. The Z/W/I electrolyte showed a significant decay with a jump in cycling up to 60 cycles, while the other two electrolytes had almost no capacity. In addition, the zinc-sulfur cell demonstrated stability for up to 1200 cycles at a current density of 3 A g^{-1} following low-current electrochemical activation in the Z/W/PM/I electrolyte. It delivered a capacity of 480 mAh g^{-1} with a capacity retention of 70 % (Figure 5i). Connecting two coin cells in series after cycling in Z/W/PM/I electrolytes can light up the LED sign (Figure 5j and Figure S31). At a lower current density of 0.5 A g^{-1}, larger volume change during the charging and discharging process led to the capacity degradation. These results indicate that the iodine source is highly correlated with sulfur utilization and the synergistic effect of PM and iodine is significantly better than electrolytes with separate components.

Discussion

In conclusion, we have successfully demonstrated an aqueous zinc-sulfur battery that combines low cost with excellent performance. This achievement was realized by strategically introducing an iodine source (ZnI_2) and adding a co-solvent (PM). To elucidate the underlying mechanism, we employed an integrated approach that included *non-in situ* electrochemistry, spectroscopic characterization, and theoretical simulation calculations. These methods allowed us to reveal the synergistic interaction between PM and ZnI_2, providing important insights into the enhancement of cell performance. The co-solvent PM regulated the solvated structure of Zn^{2+}, stabilizing water molecules and forming $[Zn(H_2O_x)PM)]^{2+}$ (x = 1-5) clusters. This reshaped the ligand structure, promoting water molecule desolvation and facilitating OTF^- decomposition to form a stable zinc anode SEI, thereby enhancing Zn^{2+} transport kinetics and interfacial compatibility. Additionally, PM participated in the reversible I^-/I_3^- reaction as an electron donor, boosting the kinetics of the sulfur cathode. The catalytic effect of the iodine source on the sulfur cathode was also investigated. Without iodine, the specific capacity (43.4 mAh g^{-1}) of zinc-sulfur batteries was less than 3 % of its theoretical capacity (1672 mAh g^{-1}) after several cycles. In contrast, the cell with ZnI_2 addition serves as a catalyst for sulfur cathodic conversion due to the reversible I^-/I_3^- reaction, facilitating the kinetics of ZnS conversion to sulfur and improving cell reversibility. The assembled aqueous zinc-sulfur batteries can provide a high capacity of 1456 mAh g^{-1} at 0.2 A g^{-1} and a high energy density of 471.8 Wh kg^{-1}, with a stability cycling performance over 1200 cycles at a current density of 3 A g^{-1}. Electrolyte structures open a pathway to develop aqueous zinc-sulfur batteries, enhancing the kinetics of

electrochemical reactions, and balancing parasitic reactions in aqueous electrolytes, paving the way for emerging battery technologies.

Author Contributions

All authors contributed to the preparation of the manuscript. G.X. conceived the idea and supervised the project. Y.G. and X.Z. developed the project concept and design. Y.G., J.Z., and X.Z. performed the material synthesis. X.Z. and C.C. guided the electrochemical testing and led data interpretation and mechanism discussion. Z.W. and T.Z. conducted the MD simulations and DFT calculations. C.C. and J.Z. assisted in editing the data graphs and manuscript. H.S. carried out the phase characterization tests.

Acknowledgements

Funding: This research is partially supported by National Key Research and Development Program of China (2022YFB3803502), and National Natural Science Foundation of China (52103076). C.C. acknowledges the support from Case Western Reserve University.

Conflict of Interest

The authors declare that they have no competing interests.

Data and materials availability: All data needed to evaluate the conclusions in the paper are present in the paper and/or the Supplementary Materials.

[1] a) F. Xie, H. Li, X. Wang, X. Zhi, D. Chao, K. Davey, S. Z. Qiao, *Adv. Energy Mater.* **2021**, *11*, 2003419; b) X. Zhu, F. Guo, C. Ji, H. Mi, C. Liu, J. Qiu, *J. Mater. Chem. A* **2022**, *10*, 12856–12868; c) C. Feng, X. Jiang, Q. Zhou, T. Li, Y. Zhao, Z. Niu, Y. Wu, H. Zhou, M. Wang, X. Zhang, M. Chen, L. Ni, G. Diao, Y. Wei, *J. Mater. Chem. A* **2023**, *11*, 18029–18045.

[2] a) M. Li, M. Liu, Y. Lu, G. Zhang, Y. Zhang, Z. Li, Q. Xu, H. Liu, Y. Wang, *Adv. Funct. Mater.* **2024**, *34*, 2312789; b) P. Cai, W. Sun, J. Chen, K. Chen, Z. Lu, Z. Wen, *Adv. Energy Mater.* **2023**, *13*, 2301279; c) S. Zhang, R. Liu, C. Streb, G. Zhang, *Polyoxometalates* **2023**, *2*, 9140037.

[3] a) Z. Xu, Y. Zhang, W. Gou, M. Liu, Y. Sun, X. Han, W. Sun, C. Li, *Chem. Commun.* **2022**, *58*, 8145–8148; b) Y. Zhao, D. Wang, X. Li, Q. Yang, Y. Guo, F. Mo, Q. Li, C. Peng, H. Li, C. Zhi, *Adv. Mater.* **2020**, *32*, 2003070; c) M. M. Gross, A. Manthiram, *ACS Appl. Mater. Interfaces* **2018**, *10*, 10612–10617; d) M. Cui, J. Fei, F. Mo, H. Lei, Y. Huang, *ACS Appl. Mater. Interfaces* **2021**, *13*, 54981–54989; e) D. Zang, Q. Li, G. Dai, M. Zeng, Y. Huang, Y. Wei, *Appl. Catal. B* **2021**, *281*, 119426.

[4] a) X. Yu, A. Manthiram, *Adv. Energy Mater.* **2017**, *7*, 1700561; b) H. Li, J. Lampkin, N. Garcia-Araez, *ChemSusChem* **2021**, *14*, 3139–3146; c) K. A. See, J. A. Gerbec, Y. Jun, F. Wudl, G. D. Stucky, R. Seshadri, *Adv. Energy Mater.* **2013**, *3*, 1056–1061; d) X. Yu, A. Manthiram, *Adv. Funct. Mater.* **2020**, *30*, 2004084; e) L. Ni, J. Gu, X. Jiang, H. Xu, Z. Wu, Y. Wu, Y. Liu, J. Xie, Y. Wei, G. Diao, *Angew. Chem. Int. Ed.* **2023**, *62*, e202306528; f) L. Ni, G. Yang, Y. Liu, Z. Wu, Z. Ma, C. Shen, Z. Lv, Q. Wang, X. Gong, J. Xie, G. Diao, Y. Wei, *ACS Nano* **2021**, *15*, 12222–12236.

[5] S. Mehta, S. Kaur, M. Singh, M. Kumar, K. Kumar, S. K. Meena, T. C. Nagaiah, *Adv. Energy Mater.* **2024**, *14*, 2401515.

[6] T. Zhou, H. Wan, M. Liu, Q. Wu, Z. Fan, Y. Zhu, *Mater. Today Energy* **2022**, *27*, 101025.

[7] a) K. N. Wang, J. W. Wang, Z. Q. Zhang, W. L. Zhang, F. Fu, Y. P. Du, *Sci. China Chem.* **2023**, *66*, 2711–2718; b) P. Hei, Y. Sai, C. Liu, W. Li, J. Wang, X. Sun, Y. Song, X. X. Liu, *Angew. Chem. Int. Ed.* **2024**, *63*, e202316082.

[8] M. Wang, H. Zhang, T. Ding, F. Wu, L. Fu, B. Song, P. Cao, K. Lu, *Sci. China Chem.* **2024**, *67*, 1531–1538.

[9] D. Liu, B. He, Y. Zhong, J. Chen, L. Yuan, Z. Li, Y. Huang, *Nano Energy* **2022**, *101*, 107474.

[10] L. Luo, C. Zhang, X. Wu, C. Han, Y. Xu, X. Ji, J. Jiang, *Chem. Commun.* **2021**, *57*, 9918–9921.

[11] G. Chang, J. Liu, Y. Hao, C. Huang, Y. Yang, Y. Qian, X. Chen, Q. Tang, A. Hu, *Chem. Eng. J.* **2023**, *457*, 141083.

[12] M. Yang, Z. Yan, J. Xiao, W. Xin, L. Zhang, H. Peng, Y. Geng, J. Li, Y. Wang, L. Liu, Z. Zhu, *Angew. Chem. Int. Ed.* **2022**, *61*, e202212666.

[13] W. Wu, S. Wang, L. Lin, H. Shi, X. Sun, *Energy Environ. Sci.* **2023**, *16*, 4326–4333.

[14] N. Chang, T. Li, R. Li, S. Wang, Y. Yin, H. Zhang, X. Li, *Energy Environ. Sci.* **2020**, *13*, 3527–3535.

[15] Z. Shi, M. Li, X. Fu, Y. Zhang, S. Jiao, Y. Zhao, *Adv. Funct. Mater.* **2024**, *34*, 2316427.

[16] a) L. Miao, R. Wang, W. Xin, L. Zhang, Y. Geng, H. Peng, Z. Yan, D. Jiang, Z. Qian, Z. Zhu, *Energy Storage Mater.* **2022**, *49*, 445–453; b) Y. Dong, N. Zhang, Z. Wang, J. Li, Y. Ni, H. Hu, F. Cheng, *J. Energy Chem.* **2023**, *83*, 324–332.

[17] P. Sun, L. Ma, W. Zhou, M. Qiu, Z. Wang, D. Chao, W. Mai, *Angew. Chem. Int. Ed.* **2021**, *60*, 18247–18255.

[18] a) X. Zhu, Z. Xu, T. Zhang, J. Zhang, Y. Guo, M. Shan, K. Wang, T. Shi, G. Cui, F. Wang, G. Xu, M. Zhu, *Adv. Funct. Mater.* **2024**, 2407262; b) X. Zhu, C. Ji, Q. Meng, H. Mi, Q. Yang, Z. Li, N. Yang, J. Qiu, *Small* **2022**, *18*, 2200055.

[19] Z. Hou, Z. Lu, Q. Chen, B. Zhang, *Energy Storage Mater.* **2021**, *42*, 517–525.

[20] T. C. Li, Y. Lim, X. L. Li, S. Luo, C. Lin, D. Fang, S. Xia, Y. Wang, H. Y. Yang, *Adv. Energy Mater.* **2022**, *12*, 2103231.

[21] R. Soni, J. B. Robinson, P. R. Shearing, D. J. L. Brett, A. J. E. Rettie, T. S. Miller, *Energy Storage Mater.* **2022**, *51*, 97–107.

[22] C. Sheng, F. Yu, C. Li, H. Zhang, J. Huang, Y. Wu, M. Armand, Y. Chen, *J. Phys. Chem. Lett.* **2021**, *12*, 2064–2071.

[23] L. Hu, Y. Chen, Y. Chen, L. Liu, S. Liang, N. Zhou, T. Ding, L. Jiang, L. Wang, X. Liang, K. Hu, *Mater. Lett.* **2024**, *357*, 135691.

[24] X. Luo, T. Xie, T. Fang, H. Liu, S. Zhang, M. Cen, W. Peng, Y. Li, X. Fan, *ACS Energy Lett.* **2023**, *8*, 3569–3577.

[25] G. Chen, Y. Kang, H. Yang, M. Zhang, J. Yang, Z. Lv, Q. Wu, P. Lin, Y. Yang, J. Zhao, *Adv. Funct. Mater.* **2023**, *33*, 2300656.

[26] a) Y. Yang, C. Liu, Z. Lv, H. Yang, Y. Zhang, M. Ye, L. Chen, J. Zhao, C. C. Li, *Adv. Mater.* **2021**, *33*, 2007388; b) S. J. Zhang, J. Hao, D. Luo, P. F. Zhang, B. Zhang, K. Davey, Z. Lin, S. Z. Qiao, *Adv. Energy Mater.* **2021**, *11*, 2102010.

[27] W. Li, K. Wang, K. Jiang, *Adv. Sci.* **2020**, *7*, 2000761.

Manuscript received: November 13, 2024
Accepted manuscript online: November 27, 2024
Version of record online: ■■, ■■

Research Article

Zinc-Sulfur Batteries

Y. Guo, X. Zhu, J. Zhang, T. Zhang, Z. Wang, M. Shan, F. Wang, C. C. Cao,* G. Xu,* M. Zhu **e202422047**

Engineering Electrolyte Network Structure for Improved Kinetics and Dendrite Suppression in Zn-S Batteries

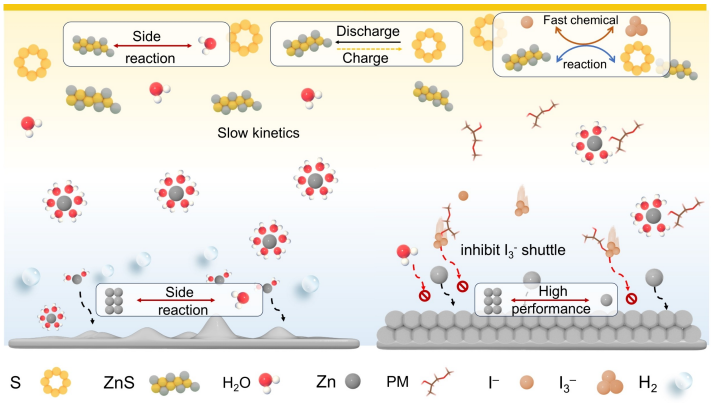

By incorporating co-solvents (PM) and additives (ZnI_2), the electrolyte network structure was optimized, enhancing the interfacial stability between the cathode and anode while promoting the reversibility of sulfur cathodic transitions. Experimental results demonstrated that PM reshaped the ligand structure, improving Zn^{2+} transport kinetics. Additionally, PM interacted synergistically with ZnI_2 to reduce cell polarization, catalyze sulfur cathode reactions, and mitigate I_3^--induced zinc anode corrosion, significantly enhancing the electrochemical performance of the aqueous zinc-sulfur battery.